

PAPER

[View Article Online](#)
[View Journal](#) | [View Issue](#)Cite this: *J. Mater. Chem. C*, 2022,
10, 2671**Tunable charge-transport polarity in
thienothiophene–bisoxindolinylidene-
benzodifurandione copolymers for
high-performance field-effect transistors†**Zihui Chen,^{‡ab} Jianyao Huang,^{‡a} Weifeng Zhang,^{‡a} Yankai Zhou,^{ab}
Xuyang Wei,^{ab} Jinbei Wei,^a Yuanhui Zheng,^a Liping Wang^c and Gui Yu^{‡ab}

N-Type semiconducting polymers are important materials for modern electronics but limited in variety and performance. To design a new n-type polymer semiconductor requires a judicious trade-off between structural parameters involving both backbone and side-chain modifications. The appeal of backbone modification emerges from the tunable electronic structures and conformational control. To control these effects typically needs installation of substituents such as halogens. In a polymer system with high molecular complexity, a few common substituents such as methyl and methoxy groups are an underdeveloped area of chemical space. In this work, we study the substituent effects in methyl- and methoxy-substituted thienothiophene–bis(oxindolinylidene)benzodifurandione copolymers on field-effect performances. The two substituents affect the conformations of the backbone and increase the frontier orbital energy levels of the polymers. Using such electronic effects, we are able to tune the charge transport behaviors from n-channel to ambipolar. This strategy allows further substitution patterns for backbone modification in other polymer semiconductors.

Received 18th June 2021,
Accepted 4th August 2021

DOI: 10.1039/d1tc02833b

rsc.li/materials-c**Introduction**

Substituent effects are ubiquitous in all facets of organic chemistry.¹ For example, bulky substituents are critical to exerting repulsive stereochemical control in asymmetric catalysis; and changing terminal substituents can promote cellular membrane permeability or add metabolic stability in drug discovery.^{2–4} In organic electronics, small-molecule and polymeric semiconductors are also benefited from the introduction of substituents which can construct targeted structures with increased mobilities and efficient charge injections. The importance of such substituent effects is magnified in tuning charge transport properties of semiconductors, because a modest modification in the molecular structure may lead to an

uncontrollable change in macroscopic parameters.⁵ Currently, modifications for screening an applicable small-molecule or polymeric semiconductor require both target- and diversity-oriented synthesis—the former one is to find a certain core that holds promise for excellent performance, and the latter one probes into its relevant chemical space, a process that typically studies substituent effects. Although the screening seems tedious and time-consuming in many cases, *ex post facto* design guidelines learned from these trial-and-error processes can rule out unfavorable candidates for further exploration.

High-mobility semiconductors are imperative in realizing modern applications, such as field-effect transistors (FETs), which promise to impact our daily life. In many applications such as logic circuits, both p- and n-type materials are needed with balanced mobilities. Although the mobilities of p-type polymeric semiconductors can rival those of amorphous or paracrystalline silicon, n-type semiconductors are still under-explored. To design a high-performance n-type semiconductor, the first concern is whether its frontier orbital energy levels match the Fermi level of the electrode. A stable electron transport material features a low-lying lowest unoccupied molecular orbital (LUMO) level close to -4.0 eV, or even lower.^{6–10} Electron-donating and -withdrawing substituents can readily tune this parameter; and in some cases, introducing such substituents is of necessity to ensure the energy levels are

^a Beijing National Laboratory for Molecular Sciences, CAS Research/Education Center for Excellence in Molecular Sciences, Institute of Chemistry, Chinese Academy of Sciences, Beijing 100190, P. R. China. E-mail: zhangwf@iccas.ac.cn, yuguai@iccas.ac.cn

^b School of Chemical Sciences, University of Chinese Academy of Sciences, Beijing 100049, P. R. China

^c School of Materials Science and Engineering, University of Science and Technology Beijing, Beijing 100083, P. R. China

† Electronic supplementary information (ESI) available. See DOI: 10.1039/d1tc02833b

‡ Z. C. and J. H. contributed equally.

located in the optimal window. Moreover, substituents can induce intra- and intermolecular interactions to rigidify the backbone, improve aggregation, and thus facilitate charge transport. Many great strides in device performance optimization have been made for unveiling the substituent effects. Despite the well-established side-chain engineering concept,^{9,11,12} backbone modification by halogen and chalcogen atoms also plays vital roles in controlling the opto-electronics properties.^{13–15} The underlying origin includes electronic and steric effects, both of which are crucial to the charge transport processes from a mechanistic perspective. The electronic effects modulate the conjugation that provides precise control over carrier injection from electrodes to the semiconductor layer, whereas the steric effects influence the self-aggregation behavior that stems from the conformations and noncovalent interactions. Although many principles have been proposed to guide the diversity-oriented design of high-mobility materials, the substituent effects in complex molecular systems are still ill-defined because of the synergy and competition between such electronic contribution, steric repulsion, and attractive noncovalent bonding. Specifically, n-type polymeric systems typically consist of electron-withdrawing functionalities that allow for efficient electron injection and in turn enhance n-channel transport. In-depth studies on substituent effects in n-type polymer semiconductors have pushed the limits of classic design concepts, and are therefore an appealing topic for electronics applications.

In this work, we choose a polymer system with high electron affinity in an effort to probe into the substituent effects on electron mobilities. The polymers are composed of a benzodifurandione-bridged indolone (NBDO) acceptor and a substituted thienothiophene (TT) donor. NBDO contains four carbonyl groups and two pyridinic nitrogen atoms that greatly stabilize the frontier orbitals. Dai *et al.* for the first time reported this building block, and obtained an NBDO-based polymer semiconductor with the highest electron mobility of $3.22 \text{ cm}^2 \text{ V}^{-1} \text{ s}^{-1}$.¹⁶ This high electron affinity unit was then used to construct other ambipolar and n-type polymers with a maximum electron mobility exceeding $7 \text{ cm}^2 \text{ V}^{-1} \text{ s}^{-1}$.^{17–19} We introduced methyl and methoxy groups to modify the structures (hereafter referred to as **DMTT** for dimethylthienothiophene and **MOTT** for dimethoxythienothiophene). Methyl substituents can tune the electronic and morphological effects in optoelectronics,^{20–22} whereas methoxy substituents are used to typically form noncovalent S...O interactions for high-performance p-type semiconductors.^{23–26} Inspired by these precedent works, we note that both the NBDO acceptor and the substituted TT donor, have nearly linear linkage sites, which enable a high degree of backbone rigidity. The major object of this work lies in the steric and electronic control by introduction of the substituents, while other important structural variables, including backbone linearity and side-chain structure, are constrained to ensure the precise comparison of these substituents. We then fabricated field-effect transistors (FETs) to describe the charge transport behaviors. The results show the substituents can raise the frontier orbital energy levels and shift the charge transport polarity, both of

which allows fine-tuning of the carrier mobilities for use in electronics.

Results and discussion

Design and synthesis

The NBDO unit has proven efficient in lowering the LUMO energy level of the polymer for electron injection; the structural modification is therefore placed on the donor moiety. To ensure the overall molecular symmetry, we introduced the substituents into 3,6-positions of thienothiophene while leaving 2,5-positions for late-stage coupling sites. We envisioned that the methyl could engage in conformational control of the backbone, whereas the electron-donating methoxy could both generate intramolecular noncovalent bonds with adjacent units and regulate the electronic effects. The attached side chains we installed on the NBDO moiety are 4-octadecyldocosyl groups, which ensure the solubility and interdigitation for the corresponding polymers.^{16,18} Scheme 1 depicts the synthetic routes to the target NBDO-based polymers. **DMTT** was accessed by the ring-closure reaction of 2,5-dihydroxy-2,5-dimethyl-3-hexyne with sulfur in high pressure reactor. **MOTT** was obtained through a copper(II) oxide-catalyzed aromatic nucleophilic reaction of 3,6-dibromothienothiophene with sodium methoxide. Both intermediates were treated with *n*-butyl lithium and quenched with trimethylstannyl chloride to afford their respective crystalline, high purity tin-containing monomers.^{25,27} The target polymers were readily obtained through the $\text{Pd}_2(\text{dba})_3/\text{P}(o\text{-tol})_3$ -catalyzed Stille copolymerization in excellent yields. The number-average molecular weights (M_n) are 54.3, 43.6, and 32.4 kDa, and polydispersity indices (\bar{D}) are 2.36, 1.72, and 1.93 for **PNBDO-TT**, **PNBDO-DMTT**, and **PNBDO-MOTT**, respectively (Fig. S1 and Table S1, ESI[†]). The 5% weight loss temperatures (Fig. S2, ESI[†]) for **PNBDO-TT**, **PNBDO-DMTT**, and **PNBDO-MOTT** are 407, 409, and 395 °C, respectively, indicating that these polymers are stable candidates for late-stage device optimization under annealing treatment (Table 1).

Optical properties

To evaluate the substituent effect on optical properties, we performed UV-visible-near infrared (UV-vis-NIR) absorption spectroscopy in the 1,2-dichlorobenzene (DCB) solutions and thin films (Fig. 1 and Table 1). All spectra show broad absorption in the range of 600–1000 nm. The absorption maximum (λ_{max}) of the unsubstituted **PNBDO-TT** in solution is located at 839 nm, and that in thin film does not shift. Nevertheless, its relative absorption intensity *versus* shoulder peaks (*ca.* 800 nm) is higher than that in solution spectrum, clearly indicating that the stronger π - π interactions or more orderly aggregation still occurs in **PNBDO-TT** thin film.^{28–30} For the **DMTT**-based polymer, the absorption maxima are 850 and 870 nm in solution and thin film, respectively. The redshift is consistent with the electronic effects that the electron-donating substituents on the donor moieties enhance the intramolecular bond polarization, leading to an increased highest occupied molecular



Polymer	M_n/D^a	λ_{max} (nm)		$E_g^{\text{opt } c}$ (eV)	E_{HOMO}^d (eV)	E_{LUMO}^d (eV)	T_{dec}^e ($^{\circ}\text{C}$)
		Soln ^b	Film				
PNBDO-TT	54.3/2.36	839	839	1.35	−5.99	−4.07	407
PNBDO-DMTT	43.7/1.72	850	870	1.31	−5.94	−4.00	409
PNBDO-MOTT	34.5/1.93	897	908	1.21	−5.75	−4.00	395

To correlate the experimental data with theoretical electronic effects and to gain insight into the steric effects, we then



Fig. 1 UV-vis-NIR absorption spectra of the three thienothiophene-bisoxindolylidene-benzodifurandione copolymers in DCB solutions and thin films.

studied the substituent effects using theoretical modeling. Because there is a pyridinic nitrogen atom proximal to the linking thiophene derivative, we envisage that noncovalent $S \cdots N$ interactions occur to reinforce the planarity of the backbone (Fig. 2). The single bond between the donor and acceptor may rotate to form two conformers. For the two possible conformers of **PNBDO-TT**, both $S \cdots N$ and $CH \cdots N$ interactions can construct planar substructures,³¹ whereas for the *S-trans* conformers of **PNBDO-DMTT** and **PNBDO-MOTT**, the lone pair of nitrogen atoms have steric repulsion with either methyl or methoxy groups. To quantify these electronic and steric effects, we calculated the energies of different conformers using potential energy scan. Simulation models were simplified using

the fragments that consist of the different donor moiety and the azaindolone subunit. The molecular geometries were optimized using density functional theory at the B3LYP/6-31G(d) level.³² The dihedral angle between two subunits was set to 0 – 180° (*syn* to *anti*) at 10° intervals, and the 0° conformer was set as the reference in the plot. Each single-point energy was further recalculated at the MP2/cc-pVDZ level to allow a more precise prediction of noncovalent interactions.³³ As shown in Fig. 3, the TT-based subunit exhibits a conventional energy diagram for highly planar molecules, with two local conformational energy minima at 0 and 180° . The $S \cdots N$ interaction leads to the energetically more stable 0° conformer. The rotational barrier of 27.5 kJ mol^{-1} indicates the significant planarization effect by the noncovalent interactions. The **DMTT**-based subunit, which contains two methyl groups on the thienothiophene, shows a smaller rotational barrier of 18.1 kJ mol^{-1} and a conformational ambiguity around the planar conformers. This simulated result is due to the repulsion between the attached methyl groups and the fused pyridine rings. The energetically disfavored repulsion competes against the $S \cdots N$ interaction, giving a detrimental effect on the overall planarity and conjugation of the backbone. The **MOTT**-based subunit also has a different conformational preference in comparison with the other two polymers. The methoxy group has an intense repulsion against the unshared electron pair of pyridinic nitrogen atoms in the 180° conformer, but strengthens the preference of the 0° conformer by formation of a weak $CH \cdots O$ interaction. These interactions give rise to an enhanced rotational barrier of 29.0 kJ mol^{-1} and a more significant energy difference between the 0 and 180° conformers.

Notably, the methoxy groups are not oriented in a uniform manner in the optimized conformation. The methoxy groups are intrinsically flexible; their conformational preference differs depending on the neighboring molecular system. To further unveil such effect, we scanned the energy distribution regarding rotation of the methoxy group (Fig. S5, ESI†). This detailed evaluation of the methoxy group reveals that both repulsion and attraction participate in the conformational control, where steric

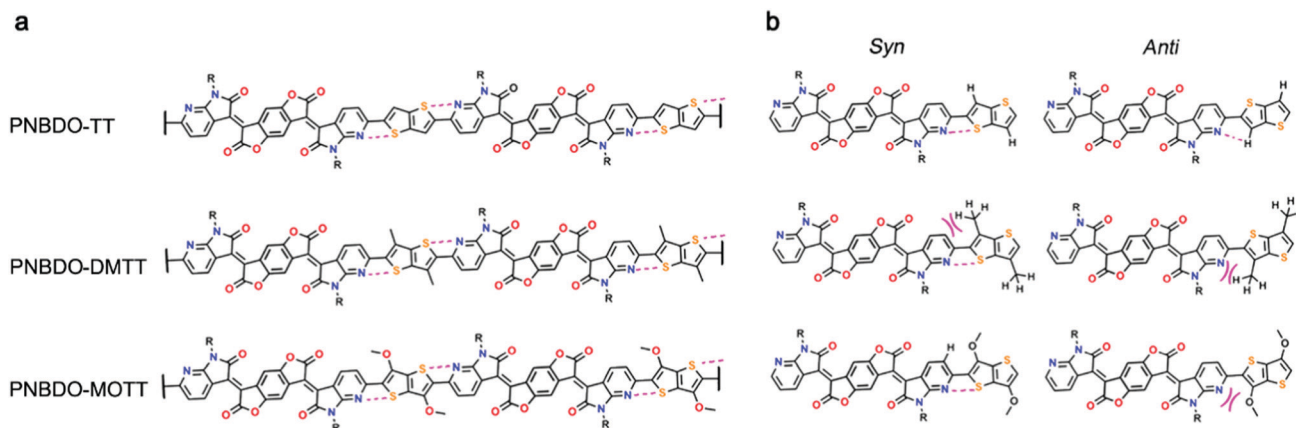


Fig. 2 Schematic illustration of noncovalent interactions and steric repulsions in the polymer system. (a) Dimeric co-repeating unit with $S \cdots N$ interactions. (b) Different conformations of a co-repeating unit with noncovalent attractions or repulsions or both.



Fig. 3 Potential energy distribution of single-bond rotation in substructures of NBDO-based polymers with different substituents. Insets are corresponding conformers at local energy minima or maxima.

interaction dominates the overall preference. We observed flexible conformations with dihedral angles in the range of 0 – 110° in the energy diagram, whatever in a **NBDO-MOTT** subunit or in an individual **MOTT**. Energetic stabilization by attractive $\text{CH}\cdots\text{O}$ interaction is tenuous because of the inferior directionality. Although the resonance effect exerts a stabilizing interaction due to electron delocalization, the repulsion between methoxy and sulfur groups in the 0° conformer slightly offsets such stabilization effect. Note that the 180° conformer shows a pronounced energy barrier due to the steric congestion twisting the co-repeating unit. These results are reasonable to clarify the overall substituent effect of methoxy groups: (1) the intrinsic flexibility of methoxy groups can affect the intermolecular packing, and (2) herein the conformational control of methoxy groups is a synergistic contribution of steric and electronic effects.

With an optimized set of torsional preferences in hand, we calculated the geometries of dimers. As expected, only methyl groups slightly twist the backbone, whereas the unsubstituted or methoxy-substituted dimers show highly planar geometries (Fig. S6, ESI[†]). The $\text{S}\cdots\text{N}$ interactions in these dimers are also confirmed by the electrostatic potential surface plot (Fig. S7, ESI[†]) and detailed reduced density gradient analyses (Fig. S8–S10, ESI[†]).^{34,35} The calculated HOMO and LUMO energy levels, as well as the tendency by substitution of methyl or methoxy groups, accord with the groups and the fused pyridine rings. The energetically disfavored repulsion competes against the $\text{S}\cdots\text{N}$ interaction, giving a detrimental effect on the overall planarity and conjugation of the backbone. The **MOTT**-based subunit also has a

different conformational preference in comparison with the other two polymers. The methoxy group has an intense repulsion against the unshared electron pair of pyridinic nitrogen atoms in the 180° conformer, but strengthens the preference of the 0° conformer by formation of a weak $\text{CH}\cdots\text{O}$ interaction. These interactions give rise to an enhanced rotational barrier of 29.0 kJ mol^{-1} and a more significant energy difference between the 0 and 180° conformers.

Field-effect transistors

We then fabricated thin-film transistors based on the three polymers using the conventional solution-processing technique. We used Corning glass as the substrate and poly(methyl methacrylate) (PMMA) as the dielectric layer. The transfer and output characteristics are illustrated in Fig. 4. We observed a typical enhancement in charge transport using thermal treatment to optimize the device performance (Fig. S11, ESI[†]). The transistors based on **PNBDO-TT** only exhibit an n-type transport behavior, whereas the devices based on the other two polymers provide n-type dominated ambipolar transport behaviors. Extracting the mobility from the saturation regimes, we calculated the average electron mobilities of 1.94 , 0.648 , and $0.0976\text{ cm}^2\text{ V}^{-1}\text{ s}^{-1}$ for the devices based on **PNBDO-TT**, **PNBDO-DMTT**, and **PNBDO-MOTT**, respectively (Table 2). The highest mobilities are 2.08 , 0.739 , and $0.103\text{ cm}^2\text{ V}^{-1}\text{ s}^{-1}$ for **PNBDO-TT**, **PNBDO-DMTT**, and **PNBDO-MOTT**, respectively. The electron mobility is in line with the electron affinity of each polymer, suggesting that a slightly destabilized frontier



Fig. 4 The transfer (a–c) and output (d and f) characteristics of the field-effect transistors based on three polymers measured under optimized conditions. (a and d) **PNBDO-TT**. (b and e) **PNBDO-DMTT**. (c and f) **PNBDO-MOTT**.

Table 2 Electrical properties of polymer based thin-film transistors

Polymer		μ_{avg}^a ($\text{cm}^2 \text{V}^{-1} \text{s}^{-1}$)	μ_{max}^b ($\text{cm}^2 \text{V}^{-1} \text{s}^{-1}$)	$I_{\text{on}}/I_{\text{off}}$	V_{TH} (V)
PNBDO-TT	n-Channel	1.94	2.08	10^3 – 10^4	43 ± 5
PNBDO-DMTT	n-Channel	0.648	0.739	10^3 – 10^4	45 ± 4
	p-Channel	0.0250	0.0255	10 – 10^2	-92 ± 5
PNBDO-MOTT	n-Channel	0.0976	0.103	10^2 – 10^3	45 ± 4
	p-Channel	0.0616	0.0711	10^3 – 10^4	-87 ± 3

^a μ_{avg} , average mobilities calculated from 10 devices. ^b μ_{max} , the maximum mobilities.

orbital suppresses electron injection. Also observed are an increased hole injection through substitution of electron-donating functionalities, with hole mobilities increased to $0.1 \text{ cm}^2 \text{V}^{-1} \text{s}^{-1}$ for the methoxy-substituted material. It is noteworthy that the ratios of hole to electron mobility are in agreement with control over frontier orbital levels, from pure n-channel (**PNBDO-TT**) to near-balanced ambipolar transport (**PNBDO-MOTT**). These results bode well for further applications in electronics.

Morphology and aggregation

The aggregation behaviors are important for intermolecular charge transport because a tightly packed chain allows faster carrier hopping in a semicrystalline, polymeric system. To detect the device optimization conditions, we first tested the surface morphology using tapping-mode atomic force microscopy (AFM) (Fig. S12, ESI†). The images all showed fiber-like grains in as-spun and annealed thin films, and the grains became larger after annealing treatment. To identify the difference in packing of the polymers with varying substituents, we performed grazing incidence wide-angle X-ray scattering (GIWAXS) measurements. Because we obtained the optimal charge

transport behaviors under thermal treatment, each sample was also tested after annealing treatment. The acquired two-dimensional (2D) and 1D diffraction patterns are provided in Fig. 5 and Fig. S13, S14 (ESI†). As shown in Fig. 5, the as-spun and annealed films of the three polymers all adopt the typical edge-on dominated packing with (*h*00) diffraction peaks up to the fourth order in the out-of-plane direction and a characteristic (010) diffraction peak in the in-plane direction. The *d*–*d* spacing, which indicate the distance between polymer backbone through alkyl-chain interactions, are estimated to be 28.2 Å for **PNBDO-TT**, 27.5 Å for **PNBDO-DMTT**, and 28.7 Å for **PNBDO-MOTT**, and increase to 28.9, 28.2, 28.9 Å, respectively (Table 3). These distances with sub-Angstrom differences infer that alkyl chains are packed in a tight, interdigitated manner. The methyl and methoxy groups on the backbone do not substantially affect the overall packing motif. The π – π spacing, indicative of the distance between polymer backbones, are estimated to be 3.43–3.44 Å for the three polymers. There are significant enhancements in (010) diffraction intensities between their respective as-spun and annealed thin films of **PNBDO-TT** and **PNBDO-DMTT**, though their π – π spacing are



Fig. 5 GIWAXS images of the **PNBDO-TT**, **PNBDO-DMTT**, and **PNBDO-MOTT** thin films.

almost the same (Fig. S14, ESI†). Therefore, the increased mobilities through thermal treatment are due mainly to the increased crystallinity. We then analyzed the coherence length using the Scherrer equation $L_c = 2\pi K/\Delta q$, where L_c is the coherence length, K is the shape factor (0.89), and Δq is the full width at the half-maximum of the (100) peak.^{36,37} In as-spun thin films, **PNBDO-TT** has a coherence length of 120 Å; this value increases to 228 Å after annealing. Likewise, the other two polymers also have enhanced crystallinities after annealing. We also calculate the paracrystalline disorder parameter (g) to confirm the tendency,^{38,39} because a reduced g factor shows a more ordered molecular packing that facilitates hopping. The g factors are estimated from the first three orders of diffraction peaks in the out-of-plane direction, and reduce from 7.38% to 4.91% for **PNBDO-TT**, from 8.05% to 6.42% for **PNBDO-DMTT**, and from 6.67% to 5.39% for **PNBDO-MOTT**, respectively, through annealing treatment. This parameter agrees with the enhanced charge transport properties.

Conclusions

In this study, we introduced two weak-to-moderate electron-donating functionalities, methyl and methoxy groups into the **PNBDO-TT** based polymers in order to explore the substituent effects on charge transport behaviors. The unsubstituted **PNBDO-TT** polymer showed a unipolar n-channel behavior with the highest electron mobility up to $2.08 \text{ cm}^2 \text{ V}^{-1} \text{ s}^{-1}$, whereas the methyl- or methoxy-substituted polymers provided ambipolar behaviors. The results indicate that the electronic effects of electron-donating groups on the donor moiety can destabilize the frontier orbitals and allow hole injection in these molecular systems. Meanwhile, although the introduced groups exert steric control over the backbone conformations, the overall packing motif does not change according to the diffraction measurements. These less bulky functional groups are potential candidates for backbone modification of complex semiconducting polymer systems to narrow the understanding gap, leverage the theoretical insight, and guide semiconductor design.

Experimental section

Material and measurements

Feedstock chemicals were purchased from Alfa, J&K, Innochem chemical or other commercial sources, and used without further purification. Anhydrous solvent (THF) was purified by distilling over sodium wire/benzophenone under inert atmosphere. (3*E*,7*E*)-3,7-bis(2-oxo-1*H*-pyrrolo[2,3-*b*]pyridin-3(2*H*)-ylidene)-benzo[1,2-*b*:4,5-*b'*]difuran-2,6(3*H*,7*H*)-dione, 2,5-bis(trimethylstannyl)thieno[3,2-*b*]thiophene, 3,6-dimethylthieno[3,2-*b*]thiophene, and 3,6-dibromothieno[3,2-*b*]thiophene were prepared following the described procedures in literatures.^{16,25,40,41} All air- and water-sensitive reactions were performed under argon atmosphere.

The ^1H NMR and ^{13}C NMR spectra of intermediates and monomers were recorded on a Bruker Fourier 300 NMR spectrometer. High temperature ^1H NMR spectra of the polymer materials were recorded on a Bruker Avance III 400 NMR spectrometer at 100 °C. Mass spectrometry (MS)/high rank mass spectrometry (HRMS) were collected on a Bruker APEXII or a 9.4 T Solarix FT-ICR mass spectrometers. High temperature gel permeation chromatography (GPC) analyses were carried out on a Polymer Labs PL 220 system (concentration: 0.10 mg mL^{-1}) using a refractive index detector at 150 °C with polystyrenes as the standard and 1,2,4-trichlorobenzene (TCB) as the eluent (flow rate: 1.00 mL min^{-1}), respectively. Elemental analyses of polymer materials were conducted on a Carlo Erba 1106

Table 3 Thin film aggregation parameters of three polymers

Polymer	d - d distance (Å)		π - π distance (Å)		Coherence length (Å)		Paracrystalline disorder parameter (g)	
	RT	Annealed	RT	Annealed	RT	Annealed	RT	Annealed
PNBDO-TT	28.2	28.9	3.44	3.44	120	228	7.38%	4.91%
PNBDO-DMTT	27.5	28.2	3.44	3.43	114	216	8.05%	6.42%
PNBDO-MOTT	28.7	28.9	3.43	3.43	173	227	6.67%	5.39%

Elemental Analyzer. Thermogravimetric analyses (TGA) were conducted on a PerkinElmer series 7 thermal analysis system under N₂ at a heating rate of 10 °C min⁻¹. Solution and thin film Absorption spectra were recorded on a Hitachi U-3010 spectrophotometer. The corresponding polymer solutions were obtained by dissolving the polymer materials in DCB and diluted to a concentration of ca. 0.03 mg mL⁻¹, while the polymer thin films were prepared on a quartz through spin-coating method. Cyclic voltammetry (CV) curves were collected on an electrochemistry workstation at room temperature with a conventional three-electrode configuration in dry acetonitrile containing 0.1 M (*n*-Bu)₄NPF₆ using Ag/AgCl electrode and Platinum wire as reference electrode, and counter electrode, respectively. A platinum stick electrode deposited with a polymer thin layer was adopted as the working electrode. Before testing, nitrogen was bubbled into the acetonitrile solution. The energy levels were calibrated using Fc⁺/Fc (−4.80 eV). All UPS spectra were acquired from an Axis-Nova CJ109, Kratos, working on a polymer thin film on silicon wafer (ca. 1 × 1 cm²), with a photoelectron energy of 21.22 eV. Theoretical calculations were performed using the Gaussian09 package. The optimization of polymer dimers is calculated at the B3LYP/6-31G(d) level. Potential energy scan was conducted at 10° intervals and the single-point energy was recalculated at the MP2/cc-pVDZ level. Reduced density gradient was analyzed by the MultiWfn package.²

Film morphology was characterized using a Digital Instruments Nanoscope V atomic force microscope operated in tapping mode. Film aggregation were analysed at BL14B1 Station of Shanghai Synchrotron Radiation Facility (SSRF). To calculate the paracrystalline disorder parameter, the following equation was used: $\Delta b = 1/d[1/N + (\pi gh)^2]$, where Δb is the integral breadth ($b = 2 \sin \theta / \lambda = q/2\pi$), N is the average number of Bragg planes, d is the d -spacing of the corresponding peak, h is the order of the diffraction peak, and g is the paracrystalline disorder parameter. The g value can be readily obtained from the slope of the Δb - h^2 plot.

3,6-Dimethylthieno[3,2-*b*]thiophene (DMTT). To an 100 mL autoclave were successively added 2,5-dihydroxy-2,5-dimethyl-3-hexyne (6.0 g, 42 mmol), elemental sulfur (3.4 g, 105 mmol), and benzene (40 mL). The autoclave was sealed and heated overnight at 200 °C. After slowly cooling to room temperature, the autoclave was carefully opened and the resulting brown residue was poured into 200 mL of H₂O and then extracted with benzene. The combined solvent was dried over anhydrous Na₂SO₄. After removal of the solvent, the crude product was purified by silica column chromatography using hexane as the eluent to give the desired product as a white crystalline solid (1.45 g, 26%). ¹H NMR (300 MHz, CDCl₃, δ): 6.93 (s, 2H), 2.34 (s, 6H). ¹³C NMR (75 MHz, CDCl₃, δ) 140.08, 130.35, 121.79, 14.62. EI-MS m/z : [M]⁺ calcd for C₆H₈S₂: 167.0. Found: 166.9.

(3,6-Dimethylthieno[3,2-*b*]thiophene-2,5-diyl)bis(trimethylstannane) (DMTT-Sn). To a solution of DMTT (1.00 g, 6.0 mmol) in dry THF (40 mL) was added 2.5 M solution of *n*-butyl lithium in hexane (6.0 mL, 15.0 mmol) was added dropwise at −78 °C. The mixture was stirred at −78 °C for another 2 h. 1.0 M solution of trimethyltin chloride in hexane

(15.5 mL, 15.5 mmol) was added in one portion. The solution was warmed to room temperature and stirred overnight. The reaction mixture was extracted with diethyl ether (3 × 60 mL). After removal of the solvent, the crude product was recrystallized from hexane twice to afford white crystals (2.45 g, 83%). ¹H NMR (300 MHz, CDCl₃, δ): 2.36 (s, 6H), 0.40 (s, 18H). ¹³C NMR (75 MHz, CDCl₃, δ) 147.60, 136.38, 134.84, 16.43, −8.18. HRMS (MALDI-TOF): calcd for C₁₄H₂₄S₂Sn₂ [M]⁺: 495.9360. Found: 495.9359.

3,6-Dimethoxythieno[3,2-*b*]thiophene (MOTT). To a 100 mL single-necked round bottle flask containing 3,6-dibromothiopheno[3,2-*b*]thiophene (2.5 g, 8.4 mmol), CuO (0.70 g, 8.4 mmol), KI (0.07 g, 0.42 mmol) was added 1.0 M NaOMe in MeOH (40 mL). The solution was heated to reflux and stirred overnight. After cooled to room temperature, the mixture obtained was poured into 200 mL of H₂O, and then extracted with dichloromethane (3 × 50 mL). The extract was washed with brine and dried over anhydrous Na₂SO₄. After removal of the solvent, the crude product was purified by silica column chromatography using hexane as the eluent to give the desired product as a colorless crystalline solid (1.15 g, 70%). ¹H NMR (300 MHz, CDCl₃, δ): 6.26 (s, 2H), 3.91 (s, 6H). ¹³C NMR (75 MHz, CDCl₃, δ) 150.8, 128.4, 97.3, 57.5. HRMS (MALDI-TOF): calcd for C₈H₈O₂S₂ [M]⁺: 199.9966. Found: 199.9968.

(3,6-Dimethoxythieno[3,2-*b*]thiophene-2,5-diyl)bis(trimethylstannane) (MOTT-Sn). The synthetic procedure of DMTT-Sn was followed using MOTT (1.00 g, 5.0 mmol), 2.5 M solution of *n*-butyl lithium in hexane (5.0 mL, 12.5 mmol), and 1.0 M solution of trimethyltin chloride in THF (13.0 mL, 13.0 mmol) to give colorless crystals (2.00 g, 71%). ¹H NMR (300 MHz, CDCl₃, δ): 3.98 (s, 6H), 0.38 (s, 18H). ¹³C NMR (75 MHz, CDCl₃, δ) 155.3, 136.1, 118.0, 59.5, −8.3. EI-MS m/z : [M]⁺ calcd for C₁₄H₂₄O₂S₂Sn₂: 525.9. Found: 525.8.

General synthetic procedure for Stille copolymerization. To a 50 mL Schlenk flask were successively added tin monomer (0.15 mmol) and NBDO-based monomer (0.15 mmol), Pd₂(dba)₃ (4.0 mg), P(*o*-tol)₃ (9.0 mg), and chlorobenzene (5.0 mL). After purged with argon for another 30 min at −78 °C, the mixture was stirred at 115 °C for 12 h. After being cooled to room temperature, the reaction mixture was poured into 200 mL methanol containing 5 mL of HCl (aq. 6 M), and stirred for 3 h. The resulting solid was filtered, and then purified *via* Soxhlet extraction in methanol, acetone, and hexane for 24 h, respectively. Finally, the solid residue was collected with DCB. After being concentrated under reduced pressure, the resulting stick solution was precipitated into methanol, filtered and dried *in vacuo* at room temperature to give the desired polymer as a film-like solid.

PNBDO-TT (233 mg, 91%). ¹H NMR (400 MHz, *d*₂-C₂D₂Cl₄, δ): 9.14–8.59 (m), 8.23 (br), 7.30–7.16 (m), 6.86 (br), 6.50–5.33 (m), 4.00–3.31 (br), 2.62–2.49 (br), 1.62–0.93 (m). GPC: M_n = 53.4 kDa, M_w = 128.8 kDa, PDI = 2.36. Elemental anal. calcd for C₁₁₀H₁₇₀N₄O₆S₂: C 77.32, H 10.03, N 3.28. Found: C 77.79, H 10.25, N 3.41.

PNBDO-DMTT (242 mg, 93%). ¹H NMR (400 MHz, *d*₂-C₂D₂Cl₄, δ): 9.16–8.56 (m), 8.31 (br), 7.32–7.20 (m), 6.86 (br),

6.53–6.34 (m), 4.01–3.33 (br), 2.61–2.16 (br), 1.60–0.92 (m). GPC: $M_n = 43.7$ kDa, $M_w = 75.3$ kDa, PDI = 1.72. Elemental anal. calcd for $C_{112}H_{174}N_4O_6S_2$: C 76.46, H 10.10, N 3.23. Found: C 76.90, H 10.33, N 3.37.

PNBDO-MOTT (238 mg, 90%). 1H NMR (400 MHz, d_2 - $C_2D_2Cl_4$, δ): 9.16–8.29 (m), 7.43–7.20 (m), 6.89 (br), 6.54–6.34 (m), 4.32–3.47 (m), 2.56–2.30 (br), 1.59–0.90 (m). GPC: $M_n = 32.5$ kDa, $M_w = 62.9$ kDa, PDI = 1.93. Elemental anal. calcd for $C_{112}H_{174}N_4O_8S_2$: C 76.05, H 9.92, N 3.17. Found: C 76.49, H 10.04, N 3.13.

Transistor fabrication and characterization

Organic field-effect transistors with a top-gate/bottom-contact configuration were fabricated on the 1.5×1.5 cm² glass slide. These substrates were sequentially cleaned by deionized water, ethanol, and acetone, and then dried by a nitrogen gun. The 30 nm-thick Au drain/source electrodes were deposited onto the glass substrates through vacuum evaporation, and the channel length/width (L/W) of 30/1400 μ m was employed. The semi-conducting and dielectric layers were fabricated by sip-coating a polymer solution (3.0 mg mL⁻¹ in DCB) and a PMMA solution (60 mg mL⁻¹ in *n*-butyl acetate) and further heating at 180 and 80 °C under nitrogen atmosphere, respectively. Eventually, an Al (80 nm) gate electrode was vacuum evaporated. A Keithley 4200 was used to explore their electrical performance under air condition. The saturation mobility was extracted from the equation: $I_{DS} = (W/2L)C_i\mu(V_{GS} - V_{th})^2$, where C_i is the capacity per unit, μ the saturation mobility, V_{GS} the gate voltage, V_{DS} the drain/source voltage, V_{th} the threshold voltage, and I_{DS} the drain/source current.

Conflicts of interest

There are no conflicts to declare.

Acknowledgements

The authors acknowledge the financial support from the National Natural Science Foundation of China (Grants 22075294, 21774134, 201905285, 22021002 and 51773016), Beijing Municipal Natural Science Foundation (Grant 2212054), and Beijing National Laboratory for Molecular Sciences (BNLMS-CXXM-202101). The GIWAXS tests were performed at BL14B1 Station of Shanghai Synchrotron Radiation Facility (SSRF). The authors thank the faculty for the assistance during the tests.

Notes and references

- 1 S. E. Wheeler, *Acc. Chem. Res.*, 2013, **46**, 1029–1038.
- 2 D. A. Nagib and D. W. MacMillan, *Nature*, 2011, **480**, 224–228.
- 3 A. Milo, A. J. Neel, F. D. Toste and M. S. Sigman, *Science*, 2015, **347**, 737–743.
- 4 K. Muller, C. Faeh and F. Diederich, *Science*, 2007, **317**, 1881–1886.
- 5 R. P. Fornari, P. W. Blom and A. Troisi, *Phys. Rev. Lett.*, 2017, **118**, 086601.
- 6 J. E. Anthony, A. Facchetti, M. Heeney, S. R. Marder and X. Zhan, *Adv. Mater.*, 2010, **22**, 3876–3892.
- 7 Y. Sui, Y. Deng, T. Du, Y. Shi and Y. Geng, *Mater. Chem. Front.*, 2019, **3**, 1932–1951.
- 8 Z. Ni, H. Wang, Q. Zhao, J. Zhang, Z. Wei, H. Dong and W. Hu, *Adv. Mater.*, 2019, **31**, 1806010.
- 9 B. Kang, R. Kim, S. B. Lee, S.-K. Kwon, Y.-H. Kim and K. Cho, *J. Am. Chem. Soc.*, 2016, **138**, 3679–3686.
- 10 T. Lei, J.-H. Dou, X.-Y. Cao, J.-Y. Wang and J. Pei, *J. Am. Chem. Soc.*, 2013, **135**, 12168–12171.
- 11 J. Mei and Z. Bao, *Chem. Mater.*, 2014, **26**, 604–615.
- 12 J. Tian, L. Fu, Z. Liu, H. Geng, Y. Sun, G. Lin, X. Zhang, G. Zhang and D. Zhang, *Adv. Funct. Mater.*, 2019, **29**, 1807176.
- 13 N. Leclerc, P. Ch  vez, O. Ibraikulov, T. Heiser and P. L  v  que, *Polymers*, 2016, **8**, 11.
- 14 Z. Fei, P. Boufflet, S. Wood, J. Wade, J. Moriarty, E. Gann, E. L. Ratcliff, C. R. McNeill, H. Sirringhaus, J. S. Kim and M. Heeney, *J. Am. Chem. Soc.*, 2015, **137**, 6866–6879.
- 15 Z. Lin, X. Liu, W. Zhang, J. Huang, Q. Wang, K. Shi, Z. Chen, Y. Zhou, L. Wang and G. Yu, *Macromolecules*, 2018, **51**, 966–976.
- 16 Y.-Z. Dai, N. Ai, Y. Lu, Y.-Q. Zheng, J.-H. Dou, K. Shi, T. Lei, J.-Y. Wang and J. Pei, *Chem. Sci.*, 2016, **7**, 5753–5757.
- 17 G. Zhang, Y. Dai, L. Qiu, K. Cho, F. Ge, H. Lee and K. C. Song, *Polym. Chem.*, 2017, **8**, 2381–2389.
- 18 K. Shi, W. Zhang, D. Gao, S. Zhang, Z. Lin, Y. Zou, L. Wang and G. Yu, *Adv. Mater.*, 2018, **30**, 1705286.
- 19 K. Huang, X. Zhao, Y. Du, S. Kim, X. Wang, H. Lu, K. Cho, G. Zhang and L. Qiu, *J. Mater. Chem. C*, 2019, **7**, 7618–7626.
- 20 Y. Ji, C. Xiao, Q. Wang, J. Zhang, C. Li, Y. Wu, Z. Wei, X. Zhan, W. Hu, Z. Wang, R. A. Janssen and W. Li, *Adv. Mater.*, 2016, **28**, 943–950.
- 21 H. S. Kim, D. Long, Y.-Y. Noh and D.-H. Hwang, *J. Mater. Chem. C*, 2018, **6**, 10464–10471.
- 22 W. Li, A. Furlan, K. H. Hendriks, M. M. Wienk and R. A. Janssen, *J. Am. Chem. Soc.*, 2013, **135**, 5529–5532.
- 23 W. Zhang, Z. Mao, J. Huang, D. Gao and G. Yu, *Macromolecules*, 2016, **49**, 6401–6410.
- 24 H. Huang, Z. Chen, R. Ponce Ortiz, C. Newman, H. Usta, S. Lou, J. Youn, Y. Y. Noh, K. J. Baeg, L. X. Chen, A. Facchetti and T. J. Marks, *J. Am. Chem. Soc.*, 2012, **134**, 10966–10973.
- 25 Z. Mao, W. Zhang, J. Huang, K. Shi, D. Gao, Z. Chen and G. Yu, *Polym. Chem.*, 2015, **6**, 6457–6464.
- 26 X. Guo, J. Quinn, Z. Chen, H. Usta, Y. Zheng, Y. Xia, J. W. Hennek, R. P. Ortiz, T. J. Marks and A. Facchetti, *J. Am. Chem. Soc.*, 2013, **135**, 1986–1996.
- 27 M. Sato, A. Asami, G. Maruyama, M. Kosuge, J. Nakayama, S. Kumakura, T. Fujihara and K. Unoura, *J. Organomet. Chem.*, 2002, **654**, 56–65.
- 28 R. S. Ashraf, I. Meager, M. Nikolka, M. Kirkus, M. Planells, B. C. Schroeder, S. Holliday, M. Hurhangee, C. B. Nielsen, H. Sirringhaus and I. McCulloch, *J. Am. Chem. Soc.*, 2015, **137**, 1314–1321.
- 29 Y. Wang, T. Hasegawa, H. Matsumoto, T. Mori and T. Michinobu, *Adv. Funct. Mater.*, 2017, **27**, 1604608.

- 30 E. Wang, Z. Ma, K. Vandewal, P. Henriksson, O. Inganäs, F. Zhang and R. A. Andersson, *J. Am. Chem. Soc.*, 2011, **133**, 14244–14247.
- 31 J. Huang, Z. Mao, Z. Chen, D. Gao, C. Wei, W. Zhang and G. Yu, *Chem. Mater.*, 2016, **28**, 2209–2218.
- 32 M. J. Frisch, G. W. Trucks, H. B. Schlegel, G. E. Scuseria, M. A. Robb, J. R. Cheeseman, G. Scalmani, V. Barone, B. Mennucci, G. A. Petersson, H. Nakatsuji, M. Caricato, X. Li, H. P. Hratchian, A. F. Izmaylov, J. Bloino, G. Zheng, J. L. Sonnenberg, M. Hada, M. Ehara, K. Toyota, R. Fukuda, J. Hasegawa, M. Ishida, T. Nakajima, Y. Honda, O. Kitao, H. Nakai, T. Vreven, J. A. Montgomery, J. E. Peralta, F. Ogliaro, M. Bearpark, J. J. Heyd, E. Brothers, K. N. Kudin, V. N. Staroverov, R. Kobayashi, J. Normand, K. Raghavachari, A. Rendell, J. C. Burant, S. S. Iyengar, J. Tomasi, M. Cossi, N. Rega, J. M. Millam, M. Klene, J. E. Knox, J. B. Cross, V. Bakken, C. Adamo, J. Jaramillo, R. Gomperts, R. E. Stratmann, O. Yazyev, A. J. Austin, R. Cammi, C. Pomelli, J. W. Ochterski, R. L. Martin, K. Morokuma, V. G. Zakrzewski, G. A. Voth, P. Salvador, J. J. Dannenberg, S. Dapprich, A. D. Daniels, Ö. Farkas, J. B. Foresman, J. V. Ortiz, J. Cioslowski and D. J. Fox, *Gaussian 09*, 2009.
- 33 N. E. Jackson, B. M. Savoie, K. L. Kohlstedt, M. Olvera de la Cruz, G. C. Schatz, L. Chen and M. A. Ratner, *J. Am. Chem. Soc.*, 2013, **135**, 10475–10483.
- 34 T. Lu and F. Chen, *J. Comput. Chem.*, 2012, **33**, 580–592.
- 35 E. R. Johnson, S. Keinan, P. Mori-Sanchez, J. Contreras-Garcia, A. J. Cohen and W. Yang, *J. Am. Chem. Soc.*, 2010, **132**, 6498–6506.
- 36 D. M. Smilgies, *J. Appl. Crystallogr.*, 2009, **42**, 1030–1034.
- 37 J. Rivnay, S. C. Mannsfeld, C. E. Miller, A. Salleo and M. F. Toney, *Chem. Rev.*, 2012, **112**, 5488–5519.
- 38 A. M. Hindleleh and R. Hosemann, *J. Phys. C: Solid State Phys.*, 1988, **21**, 4155–4170.
- 39 R. Noriega, J. Rivnay, K. Vandewal, F. P. V. Koch, N. Stingelin, P. Smith, M. F. Toney and A. Salleo, *Nat. Mater.*, 2013, **12**, 1038–1044.
- 40 J. Chantson, H. Görls and S. Lotz, *J. Organomet. Chem.*, 2003, **687**, 39–45.
- 41 J. Nakayama, H. Dong, K. Sawada, A. Lshii and S. Kumakura, *Tetrahedron*, 1996, **52**, 471–488.